applied sciences

MDPI

Article

Study on Hydrochemical Characteristics and Evolution Patterns of Roof Sandstone Water in the Banji Coal Mine

Nayu Xu, Yu Liu *, Qimeng Liu *, Gui Sun and Qiding Ju

School of Earth and Environment, Anhui University of Science & Technology, Huainan 232001, China; nayuxu@163.com (N.X.); gsunlanze@163.com (G.S.); qdju@aust.edu.cn (Q.J.)
* Correspondence: yliu@aust.edu.cn (Y.L.); qmliu_1972@126.com (Q.L.)

Abstract

The Banji Mine, located in the western part of the Huainan Coalfield, is characterised by a deep burial depth and multiple aquifers. It faces significant water inflow risks from roof aquifers, especially from the sandstone aquifer above the No. 9 coal seam. To explore the hydrochemical evolution of this sandstone aquifer and address key scientific challenges in water hazard prevention, an integrated approach combining mathematical statistics, Piper trilinear diagrams, Gibbs diagrams, and principal component analysis (PCA) was employed. Results show that from 2020 to 2023, the average TDS increased from 1729.51 mg·L^{-1} to 2061.22 mg·L^{-1}, and the hydrochemical types transitioned from a mix of Cl-Na (48.6% of samples) and HCO_3·Cl-Na to a dominant Cl-Na type (91.1% in 2023), exhibiting high mineralisation and a distinct trend of water salinisation. The dissolution of evaporites and evaporative concentration were identified as the primary processes influencing the hydrochemical characteristics, with PCA indicating that the dominant factor (F1) explained 66.269% of the variance. Saturation index (SI) analysis revealed that calcite and dolomite were saturated to supersaturated (SI: 0.73–2.15 and 1.66–4.81, respectively), while gypsum and halite were undersaturated but showed a tendency to dissolve towards equilibrium. Over time, the cation exchange and sulfate reduction processes weakened, indicating that mining activities have disrupted the hydrochemical equilibrium of the roof sandstone aquifer, accelerating water salinisation. This study provides a theoretical foundation for identifying the causes and early warning signs of water hazards in the roof strata of the Banji Mine.

Keywords: cluster analysis; groundwater; principal component analysis; water chemical characteristics; water–rock interaction

Check for updates

Academic Editor: Fernando Rocha

Received: 20 December 2025
Revised: 9 January 2026
Accepted: 12 January 2026
Published: 14 January 2026

Copyright: © 2026 by the authors. Licensee MDPI, Basel, Switzerland. This article is an open access article distributed under the terms and conditions of the Creative Commons Attribution (CC BY) license.

1. Introduction

In recent years, with the increasing depletion of shallow coal resources, water hazard issues in deep coal seam mining have become a significant threat, particularly those related to water inrushes from coal-measure sandstone aquifers [1,2]. Sandstone water hazards, as the primary source of water influx, are typically characterised by large water inflow volumes and high water pressures. Moreover, these aquifers are often hydraulically connected to overlying strong aquifers, making them prone to water inrush accidents that can lead to severe consequences [3], such as flooding of working faces or even the entire mine shaft. Analysing and understanding these hazards is essential for preventing and controlling water-related risks in deep mining.

Recently, hydrogeochemical methods have gained prominence in identifying the sources of water inrushes. Traditional graphical methods, such as the Piper trilinear diagram and Gibbs diagram, are widely used to distinguish hydrochemical types and control processes of groundwater. Ion ratio coefficients can serve as indicators for water–rock interactions and cation exchange [4,5]. Principal component analysis (PCA) is effective in extracting various factors influencing water quality evolution from large hydrochemical datasets, aiding in the identification of different hydrogeochemical processes [6]. Both domestic and international scholars continue to explore hydrogeological discrimination methods. For example, Jiacong Tian et al. utilised Piper diagrams, ion ratio methods to investigate the hydrochemical characteristics and genesis of groundwater in the Liuzhuang coal Mine and analysed the Fluoride Release Mechanism [7]. Qiling Jiang et al. employed multivariate statistical analysis, Piper trilinear diagrams, and ion ratio coefficients to examine the hydrochemical characteristics and formation mechanisms of sandstone water in the Liuzhuang coal Mine [8]. Lijuan Yuan et al. applied mathematical statistics, Piper diagrams, Gibbs diagrams, and ion ratios to study the Hydrochemical zonation in Beijing City, exploring the evolution patterns and causes of hydrochemical characteristics from both temporal and spatial perspectives [9]. Fengxia Liu et al., using the Ningtiaota coal mine as a case study, employed Piper diagrams, Gibbs diagrams, and major ion concentration relationship diagrams to analyse the hydrochemical characteristics and origins of hydrochemical components in the wellfield's aquifers. They further examined the genesis and sources of hydrochemical components using ion concentration comparisons [10]. Abdulrahman Shuaibu was the first to apply the Ionic Balance Error (IBE) method to assess the accuracy of water quality data, subsequently using Gibbs diagrams and Piper trilinear diagrams to investigate the hydrogeochemical characteristics and drinking suitability of groundwater resources in the Komadugu-Yobe basin, located in the Sahel region [11].

The Banji Mine, developed as the second mine in the new area by China Coal Xinji Energy Co., Ltd., has limited research on its groundwater. A comprehensive analysis of the hydrochemical characteristics and evolution patterns of the sandstone aquifer (referred to as "sandstone water") in the coal seam roof is still lacking. As the sandstone water above the No. 9 coal seam serves as the primary water-filling source for the Banji Mine, studying its chemical composition, variation trends, and influencing factors is essential. This study, based on existing data and measurement results, employed SPSS 2022 software for statistical analysis of hydrochemical parameters, origin software to generate Piper trilinear diagrams, and Origin 2024 software to construct Gibbs diagrams and major ion relationship diagrams. Furthermore, PCA was performed on these hydrochemical characteristics. In contrast to previous studies, this research utilised the geochemical modelling software PHREEQC (Version 3.8.6-17100) to calculate the SI of various minerals in water samples from different years and analysed them to predict hydrochemical evolution trends. By applying these methods, this study systematically analysed the hydrochemical characteristics, temporal evolution patterns, and causes of evolution of the No. 9 coal seam roof sandstone water in the Banji Mine, providing a scientific basis for effective water hazard control in the mine.

2. Geological Setting of the Study Area

2.1. Overview of the Study Area

The Banji Coal Mine is located at the junction of Lixin County (Bozhou City), Yingshang County, and Yingdong District (Fuyang City) in Anhui Province, under the administrative jurisdiction of Huji Town, Lixin County. It is situated approximately 25 km north of Lixin County's urban area and about 30 km south of Yingshang County's urban area. The mine field extends approximately 6.0 km from east to west, with a width ranging from 4.0 km to 7.0 km from north to south, covering a total area of 33.6 km^2.

The study area lies in the western part of the hydrogeological zoning of the Huainan Coalfield, with the mine's hydrogeological conditions controlled by regional factors. The aquifer and aquifuge systems consist primarily of the Cenozoic unconsolidated layer aquifers and aquifuges, the Permian aquifer-aquifuge system, the Carboniferous aquifer-aquifuge system, and the Ordovician limestone aquifer. These can be divided into four aquifers and three aquifuges, with thickness increasing from south to north, following the paleotopography.

The direct water-filling aquifer for the 110504 working face (Figure 1) is the sandstone aquifer in the roof of the No. 9 coal seam. A relatively close hydraulic connection exists between this sandstone aquifer and the lower fourth aquifer (Quaternary aquifer) of the Cenozoic unconsolidated porous aquifer. The water-filling intensity mainly depends on the recharge strength from the Cenozoic fourth aquifer. Two relatively continuous sandstone layers are developed in the roof of the No. 9 coal seam.

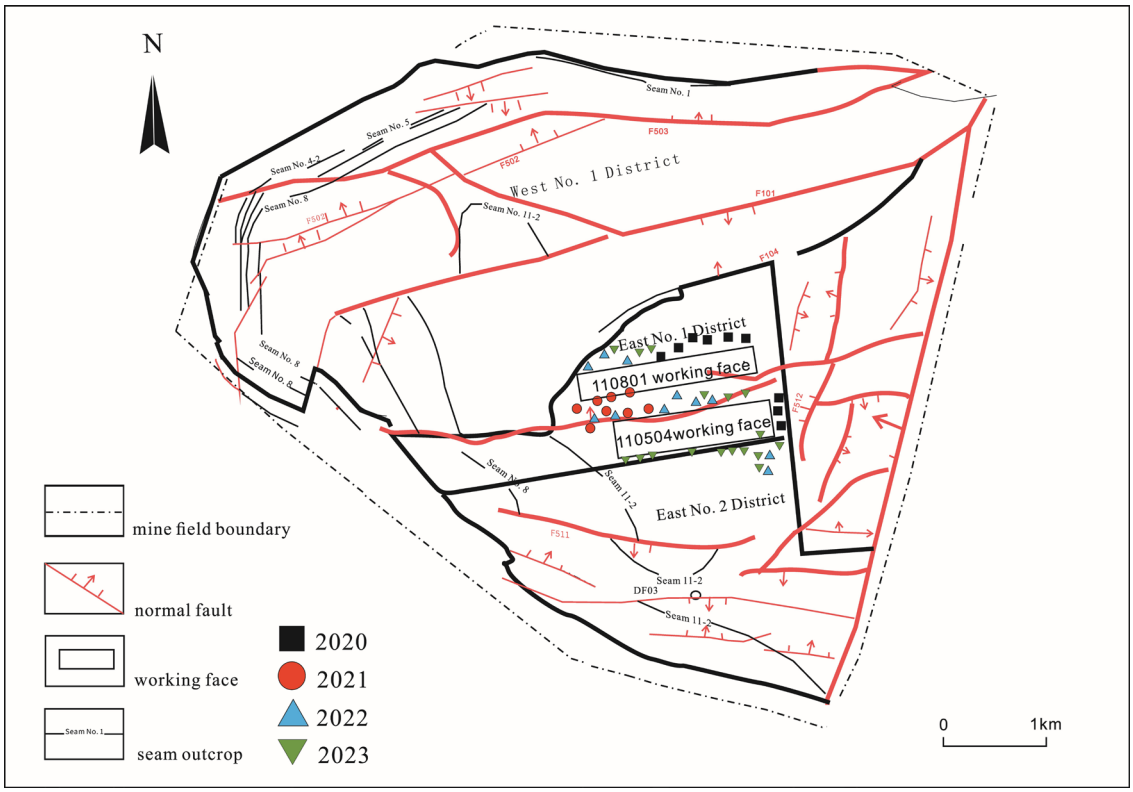


Figure 1. Mine structures, working face distribution, and hydrogeochemical sampling locations of the study area.

The lower sandstone layer, with a thickness ranging from 7.1 to 21.9 m (average 11 m), is composed of one to three layers of fine to medium-grained sandstone, often containing siderite nodules. Local fractures are developed and filled with calcite.

The upper sandstone layer, with a thickness ranging from 1.8 to 14 m (average 11.9 m), is primarily composed of medium-grained quartz sandstone, with relatively developed fractures.

The water yield property of this aquifer is mainly influenced by the development degree, aperture size, and extension length of the sandstone fractures. It is characterised by a heterogeneous water yield capacity, predominantly static storage consumption, and is generally considered weakly water-yielding.

2.2. Sampling and Testing

To investigate the hydrochemical background of the roof sandstone water in the Banji Mine, systematic sampling of the No. 9 coal seam roof sandstone aquifer was conducted from March 2020 to December 2023. A total of 202 groundwater samples were collected (37 in 2020, 26 in 2021, 60 in 2022, and 79 in 2023). The spatial distribution of all sampling points is plotted in Figure 1, providing a basis for assessing the spatial characteristics of the hydrochemical evolution.

The collection of groundwater samples and the subsequent laboratory analysis of water quality indicators strictly adhered to the guidelines of the Geological and Mineral Industry Standard of the People's Republic of China (Methods for Examination of Groundwater Quality, DZ/T) [12] and the relevant Coal Industry Standard of the People's Republic of China (MT/T) [13]. This protocol ensured the standardisation and comparability of all generated data.

3. Research Methods

3.1. Characteristics of Hydrochemical Composition

Statistical analysis was conducted on the conventional hydrochemical parameters of water samples from the No. 9 coal roof sandstone aquifer (Table 1). The results showed that the average concentration order of cations in the study area for 2020, 2021, and 2022 was $Na^+ + K^+ > Mg^{2+} > Ca^{2+}$, while in 2023, it was $Na^+ + K^+ > Ca^{2+} > Mg^{2+}$. $Na^+ + K^+$ were overwhelmingly dominant, accounting for 95.32%, 95.6%, 94.5%, and 94.4% of the total cations, respectively. The average concentration order of anions consistently followed $Cl^- > HCO_3^- > SO_4^{2-}$, with Cl^- and HCO_3^- being the most abundant, representing 93.32%, 93.84%, 89.43%, and 87.00% of the total anions, respectively. The pH values of the sandstone water ranged from 7.9 to 8.204 in each year, indicating weakly alkaline water.

Table 1. Statistical summary of hydrochemical parameters of sandstone water in the study area.

Period	Parameter	Mass Concentration (mg·L^{-1})							pH
		$Na^+ + K^+$	Ca^{2+}	Mg^{2+}	SO_4^{2-}	Cl^-	HCO_3^-	TDS	
2020 (n = 37)	Maximum	772	37.1	92.73	294.29	961.08	1491.57	2174.99	8.54
	Minimum	499.37	2.09	0.58	0	253.24	263.02	1247.01	7.55
	Average	653.88	21.83	10.21	88.54	646.66	591.12	1729.51	7.9
	Std. Dev	97.75	12.8	14.44	80.56	273.06	273.95	331.27	0.22
	Cv	14.90%	58.60%	141.40%	91%	42.20%	46.30%	19.2%	2.80%
2021 (n = 26)	Maximum	816.75	36.61	94.26	203.78	1023.3	739.75	2238.38	9.78
	Minimum	405.37	4.07	3.03	0	318.82	63.3	1062.43	7.66
	Average	610.38	17.42	11	72.7	635.71	471.78	1608.75	8.204
	Std. Dev	126.63	10.23	16.96	61.21	240.70	132.91	369.95	0.49
	Cv	20.70%	58.70%	154.10%	81%	37.90%	28.20%	23%	5.90%
2022 (n = 60)	Maximum	859.63	46.05	92.32	226.7	1091.86	994.63	2548.96	8.35
	Minimum	333.31	5.75	4.66	0	296.01	219.67	888.31	7.41
	Average	747.49	30.46	12.775	153.32	881.31	415.11	2042.52	7.98
	Std. Dev	102.45	9.71	11.56	66.62	218.51	198.71	319.63	0.19
	Cv	13.70%	31.90%	87.90%	43.50%	24.80%	47.90%	15.60%	2.30%
2023 (n = 79)	Maximum	1064.35	58.87	25	384.15	1090.87	1459.11	2808.44	12.08
	Minimum	362.67	3.95	1.49	9.46	284.88	35.51	985.86	7.28
	Average	750.32	31.5	12.87	185.8	904.91	338.57	2061.22	8.09
	Std. Dev	91.65	8.75	3.76	44.18	164.59	180.91	255.87	0.64
	Cv	12.20%	27.80%	29.20%	23.80%	18.20%	53.40%	12.40%	7.90%

Total Dissolved Solids (TDS) showed average values of 1729.51 mg·L^{-1}, 1608.75 mg·L^{-1}, 2042.52 mg·L^{-1}, and 2061.22 mg·L^{-1}, respectively, with a slight decrease in TDS in 2021 but a general increasing trend thereafter. Regarding spatial variability, Mg^{2+} and SO_4^{2-} both exhibited high coefficients of variation (Cv) but demonstrated contrasting environmental behaviours. Mg^{2+} maintained a consistently low mean concentration (ranging from 10.21 to 12.87 mg·L^{-1} across the years) yet showed exceptionally high variability (e.g., Cv up to 154.10% in 2021, with a standard deviation of 16.96 mg^{-1}). This "high-variability, low-concentration" signature suggests that its source (e.g., dolomite dissolution) is likely highly localised, controlled by specific lithology or micro-geochemical environments. However, as its absolute concentration is significantly lower than that of $Na^+ + K^+$ and Ca^{2+}, its influence on the dominant hydrochemical type remains minor. In contrast, SO_4^{2-} demonstrated a clear and steady concentration increase from 88.54 mg·L^{-1} in 2020 to 185.80 mg·L^{-1} in 2023. Concurrently, its spatial variability decreased substantially, with the Cv dropping from 91% to 23.8% and the standard deviation evolving from 80.57 to 44.22 mg·L^{-1}. This inverse pattern—rising concentration alongside declining variability—suggests the progressive homogenization of a sulfate source within the aquifer, likely driven by widespread oxidation of sulfide minerals (e.g., pyrite) accelerated by mining activities.

3.2. Hydrochemical Types

The Piper trilinear diagram, a common tool for analysing hydrochemical characteristics and evolution patterns [14,15], revealed complex hydrochemical types in the study area (Figure 2). Temporally, in 2020, 48.6% of the roof sandstone water samples were classified as the Cl-Na hydrochemical type. Initially, the groundwater exhibited a coexistence of Cl-Na and HCO_3·Cl-Na types, but over time, the groundwater transitioned to a dominant Cl-Na hydrochemical type. By 2023, 91.1% of the samples were classified as Cl-Na. This shift suggests that the dominant geochemical processes in the groundwater environment have become more consistent, likely due to intense evaporative concentration or continuous sources of Cl^- and Na^+.

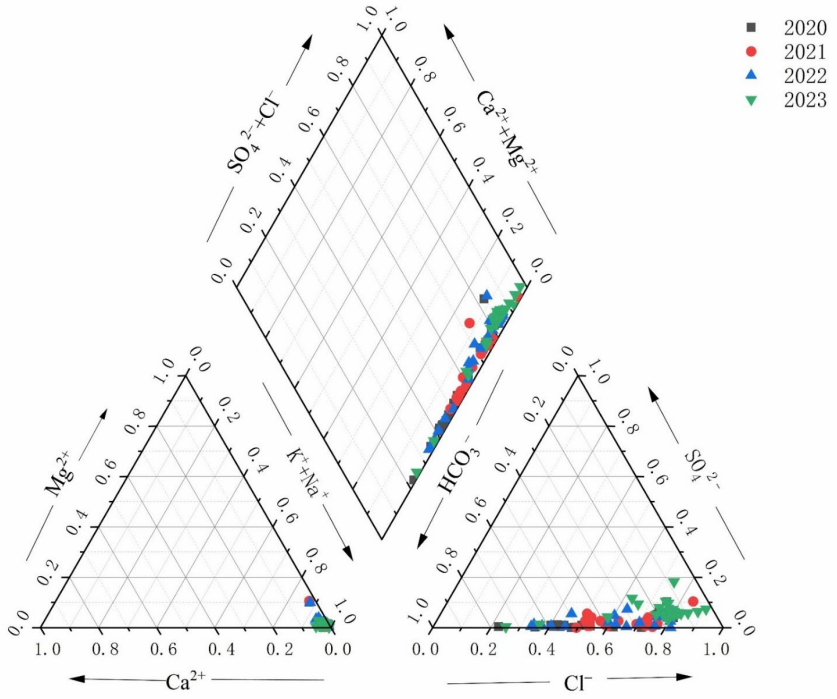


Figure 2. Piper trilinear diagram of water samples from the study area.

3.3. Mechanisms of Groundwater Hydrochemical Evolution

3.3.1. Ion Correlation Analysis

The Pearson correlation index, introduced by Pearson, is a useful tool for revealing the hydrochemical characteristics of groundwater and their formation mechanisms. In this study [16], Pearson correlation analysis of hydrochemical components was conducted using SPSS software (Table 2). The results indicated that TDS showed significant positive correlations with all major ions except HCO_3^-. A strong positive correlation was observed between $Na^+ + K^+$ and Cl^-, suggesting a common source, likely related to the dissolution of salt rock. The strong positive correlation between Ca^{2+} and Cl^- further suggests that, in addition to salt rock dissolution, the dissolution of calcium-containing evaporites may also be involved. In contrast, HCO_3^- exhibited significant negative correlations with major ions such as Cl^-, SO_4^{2-}, and Ca^{2+}. Notably, the correlation coefficient between HCO_3^- and SO_4^{2-} was −0.693, supporting the hypothesis of sulfate reduction occurring in the system.

Table 2. Correlation matrix of major parameters in sandstone water from the study area.

Elements	$Na^+ + K^+$	Ca^{2+}	Mg^{2+}	SO_4^{2-}	Cl^-	HCO_3^-	TDS	pH
$Na^+ + K^+$	1							
Ca^{2+}	0.758 **	1						
Mg^{2+}	0.274 **	0.303 **	1					
SO_4^{2-}	0.715 **	0.686 **	0.238 **	1				
Cl^-	0.892 **	0.884 **	0.311 **	0.768 **	1			
HCO_3^-	−0.375 **	−0.619 **	−0.177 *	−0.693 **	−0.705 **	1		
TDS	0.986 **	0.826 **	0.328 **	0.772 **	0.936 **	−0.46 *	1	
pH	−0.226 **	−0.358 **	−0.152 *	0.014	−0.291 **	0.002	−0.286 **	1

Note: * and ** indicate significant correlation at the 0.01 and 0.05 levels, respectively.

The Gibbs model, used to identify the controlling mechanisms of the hydrochemical composition of sandstone water [17,18], includes processes such as evaporative concentration, rock weathering, and atmospheric precipitation. Gibbs diagrams (Figure 3), plotting $Na^+/(Na^+ + Ca^{2+})$ and $Cl^-/(Cl^- + HCO_3^-)$ on the x-axes and the logarithm of TDS on the y-axis, show that the majority of water sample data points from 2020 to 2023 fall within the evaporative concentration domain. This indicates that the roof sandstone water in the Banji Mine has undergone intense evaporative concentration. Moreover, in Figure 3b, the data points progressively shift towards the positive direction of the $Cl^-/(Cl^- + HCO_3^-)$ x-axis over time, suggesting a continuous strengthening of the evaporative concentration effect on the hydrochemical composition. This trend is associated with the observed decrease in HCO_3^- concentration over time.

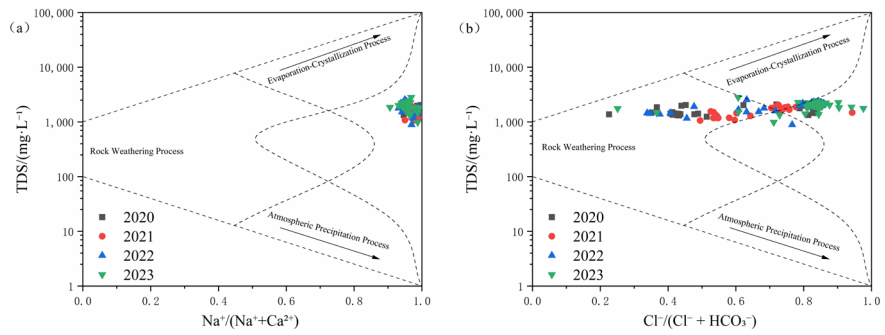


Figure 3. Gibbs diagrams of sandstone water in the study area: (**a**) Gibbs diagram based on the ratio of $Na^+/(Na^+ + Ca^{2+})$; (**b**) Gibbs diagram based on the ratio of $Cl^-/(Cl^- + HCO_3^-)$.

Under natural conditions, water–rock interactions generate various ions in groundwater and rock formations. Analysing the ratio relationships of these ions offers further insights into the groundwater formation mechanisms. The ionic composition of groundwater was analysed using the ratios of Mg^{2+}/Na^{+}, HCO_3^{-}/Na^{+}, and Ca^{2+}/Na^{+} to investigate the influence of carbonate rocks, silicate rocks, and evaporites on water quality. As shown in Figure 3, the water sample points are primarily distributed within the evaporite domain. Additionally, in Figure 4b, the data points show a clear trend towards the evaporite field over time. This indicates that the water–rock interactions in the aquifer of the study area are primarily controlled by evaporite dissolution, with minimal influence from silicate rocks and nearly no impact from carbonate rocks. Furthermore, the controlling effect of evaporites has become more pronounced over time.

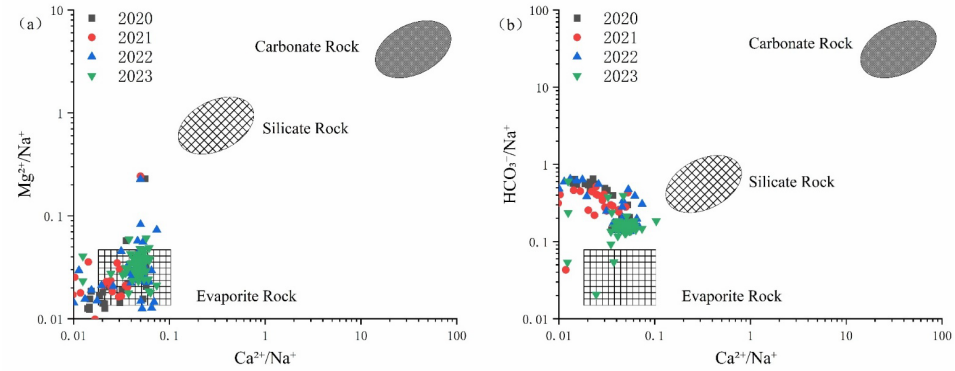


Figure 4. Relationship between meq/L ratios of Ca^{2+}/Na^{+} and other ions in groundwater of the study area: (**a**) Mg^{2+}/Na^{+} vs. Ca^{2+}/Na^{+}; (**b**) HCO_3^{-}/Na^{+} vs. Ca^{2+}/Na^{+}.

3.3.2. Analysis of Major Ion Controls and Sources

The water quality of the sandstone aquifer in the study area is primarily influenced by evaporative concentration and evaporite dissolution, as indicated by the previous results. Analysing ionic ratios provides valuable insights into the dominant controlling factors affecting groundwater chemistry [19,20].

(1) The ratio $Cl^{-}/(K^{+} + Na^{+})$ is useful for identifying the primary source of K^{+} and Na+ in groundwater. When $Cl^{-}/(K^{+} + Na^{+})$ equals 1, it suggests that K^{+} and Na^{+} originate predominantly from halite dissolution [21]. In Figure 5a, data points cluster near the 1:1 line, implying that halite dissolution is the dominant process. However, the points are systematically distributed below the 1:1 line, indicating that K^{+} and Na^{+} in the study area are not solely derived from halite dissolution but are also influenced by other factors, potentially including the dissolution of sodium- and potassium-containing silicate minerals or cation exchange.

(2) The sources of Ca^{2+} and SO_4^{2-} are primarily linked to gypsum. A 1:1 molar ratio between these ions suggests that gypsum dissolution releases equivalent molar amounts of Ca^{2+} and SO_4^{2-} into the water, as described by the dissolution equation: $CaSO_4 \cdot 2H_2O \rightleftharpoons Ca^{2+} + SO_4^{2-} + 2H_2O$. In Figure 5b, most data points lie above the 1:1 line, indicating that SO_4^{2-} concentrations generally exceed those of Ca^{2+}. This suggests the presence of additional SO_4^{2-} sources, such as the dissolution of other sulfate minerals or the oxidation of pyrite (e.g., $2FeS_2 + 7O_2 + 2H_2O \rightarrow 2Fe^{2+} + 4SO_4^{2-} + 4H^{+}$).

(3) The dissolution of dolomite and calcite typically results in Ca^{2+} to HCO_3^{-} molar ratios of approximately 4:1 and 2:1, respectively, as represented by the following reactions: $CaCO_3 + H_2O + CO_2 \rightarrow Ca^{2+} + 2HCO_3^{-}$ and $CaMg(CO_3)_2 + 2H_2O + 2CO_2(g) \rightarrow Ca^{2+} + Mg^{2+} + 4HCO_3^{-}$. However, Figure 5c shows that most data points lie above the 2:1 line, indicating a minor contribution from calcite dissolution. Many

points are clustered near the 4:1 line, suggesting a potential source from dolomite dissolution. Nevertheless, a significant number of points are above the 4:1 line, implying an additional source of HCO_3^-, likely linked to cation exchange or sulfate reduction processes.

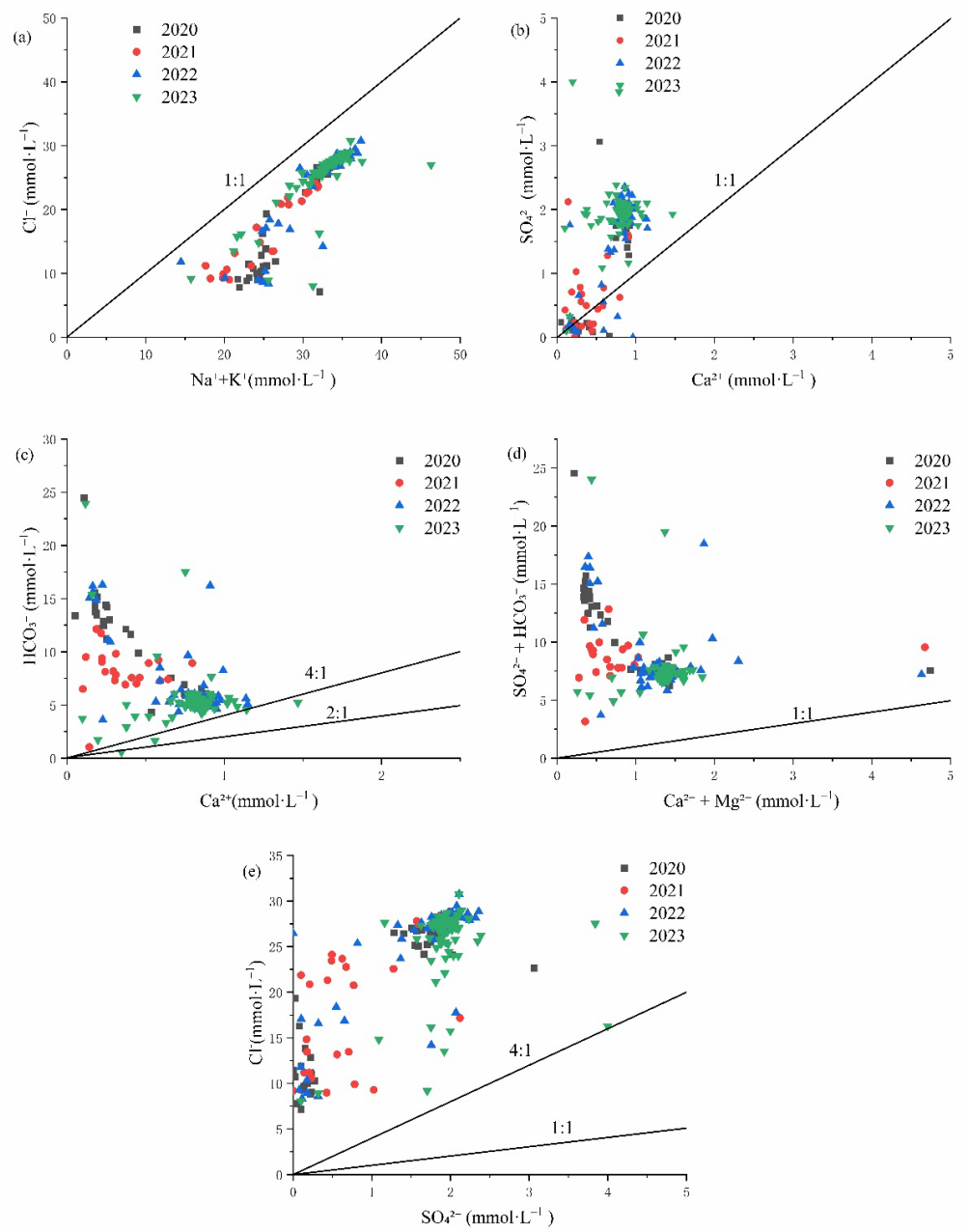


Figure 5. Ion ratio analysis diagrams of groundwater in the study area: (**a**) Cl^- vs. $Na^+ + K^+$; (**b**) SO_4^{2-} vs. Ca^{2+}; (**c**) HCO_3^- vs. Ca^{2+}; (**d**) $SO_4^{2-} + HCO_3^-$ vs. $Ca^{2+} + Mg^{2+}$; (**e**) Cl^- vs. SO_4^{2-}.

(4) In natural waters, Ca^{2+} and Mg^{2+} primarily originate from the weathering and dissolution of carbonates (e.g., calcite, dolomite), silicates (e.g., K-feldspar, plagioclase), and evaporites (e.g., gypsum). Therefore, the meq·L^{-1} ratio of ($Ca^{2+} + Mg^{2+}$) to ($SO_4^{2-} + HCO_3^-$) can provide insight into the sources of these ions. A ratio of $(SO_4^{2-} + HCO_3^-)/(Ca^{2+} + Mg^{2+}) < 1$ suggests a dominant contribution from carbonate dissolution. A ratio of 1 indicates that both carbonate and evaporite (e.g., gypsum) dissolution are involved [22], while a ratio > 1 suggests dissolution primarily from silicate and evaporite minerals. In Figure 5d, all data points are situated above the

1:1 line, indicating that SO_4^{2-} + HCO_3^- are insufficient to balance Ca^{2+} + Mg^{2+}. This suggests that silicate and evaporite dissolution, possibly in combination with some cation exchange, is the primary source.

(5) The Cl^-/SO_4^{2-} ratio can be used to assess the intensity of sulfate reduction in water samples. Under anaerobic conditions, certain microorganisms utilise organic matter as an energy source and reduce sulfate to hydrogen sulfide: SO_4^{2-} + 2C + $2H_2O$ → H_2S + $2HCO_3^-$. The exceptionally high Cl^-/SO_4^{2-} ratio observed in the study suggests significant sulfate reduction, which is supported by relatively high HCO_3^- concentrations from 2020 to 2022, as seen in Figure 5c. This provides strong evidence of sulfate reduction activity. However, the overall decrease in HCO_3^- concentration, coupled with an increase in SO_4^{2-} concentration from 2020 to 2023, indicates a weakening of sulfate reduction. This is likely due to mining activities at the Banji Mine, which introduced oxygen-rich water into the previously confined aquifer, disrupting the reducing environment and inhibiting or even eliminating the obligate anaerobic sulfate-reducing bacteria. Specifically, this transition was primarily attributed to new fracture networks formed by mining activities, which provided direct channels for oxygenated atmospheric water to enter the deep aquifer, significantly increasing the dissolved oxygen concentration and thereby inhibiting the activity of sulfate-reducing bacteria. Additionally, minor cross-formational recharge from overlying shallow aquifers with toxic groundwater might also play a secondary role, but the former is the dominant mechanism causing the disruption of the reducing environment.

3.3.3. Cation Exchange Adsorption

Cation exchange adsorption refers to the ion exchange process occurring between the negatively charged surfaces of rock or soil particles and cations in groundwater. As water moves through the aquifer media, cations adsorbed on the surface of the media are exchanged with those in the water, resulting in changes to the water's ionic composition [23]. This process is assessed using the ratio $\gamma(HCO_3^- + SO_4^{2-} - Mg^{2+} - Ca^{2+})/\gamma(Na^+ + K^+ - Cl^-)$. A ratio close to −1 indicates significant cation exchange adsorption. In the provided diagram, the data points from the four-year period are tightly distributed along the 1:1 line, confirming the presence of cation exchange adsorption throughout the sandstone aquifer in the study area.

The Chloro-Alkaline Indices (CAI-1 and CAI-2) are additional indicators used to further assess the cation exchange process in the study area's groundwater, specifically the exchange between sodium ions and calcium/magnesium ions [24].

The Chloro-Alkaline Indices (CAI-1 and CAI-2) were calculated using the following formulae to assess cation exchange processes:

$$\text{CAI-1} = \frac{\gamma(Cl^-) - \gamma(Na^+ + K^+)}{\gamma(Cl^-)}$$

$$\text{CAI-2} = \frac{\gamma(Cl^-) - \gamma(Na^+ + K^+)}{\gamma(HCO_3^-) + \gamma(SO_4^{2-})}$$

where γ represents the equivalent concentration of the respective ions in milliequivalents per litre (meq·L^{-1}). When both CAI-1 and CAI-2 values are less than 0, forward cation exchange occurs, where Na^+ and K^+ from the aquifer are replaced by the adsorption of Ca^{2+} and Mg^{2+} into the water. Conversely, values greater than 0 indicate reverse cation exchange. The higher the absolute values of these indices, the more intense the cation exchange process [25].

The results indicate that all data points from the water samples in the study area fall within the negative region of the CAI-1 and CAI-2 plots (Figure 6), showing that both CAI-1 and CAI-2 are less than 0. This confirms that Ca^{2+} and Mg^{2+} in the groundwater replace Na^{+} and K^{+} from the surrounding aquifer rocks, signifying a forward cation exchange process [26]. Moreover, the data points shift toward the origin, suggesting a gradual weakening of the forward cation exchange over time.

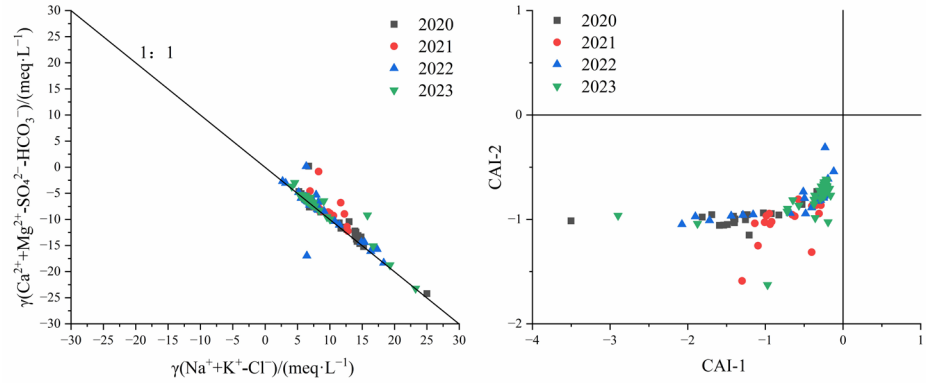


Figure 6. Correlation diagram of cation exchange in the study area.

3.3.4. Saturation Index Analysis

The hydrogeochemical simulation software PHREEQC can be utilised to calculate the SI of various minerals in groundwater. By analysing changes in SI values, it is possible to identify different stages of hydrochemical evolution and assess the intensity of evaporation effects on groundwater [27]. A positive SI value indicates a tendency for mineral precipitation, while an SI of zero signifies equilibrium between dissolution and precipitation. A negative SI suggests that the mineral is more likely to dissolve. An SI range of 0 ± 0.5 is generally considered to represent an equilibrium state. As previously noted, the sandstone water in the study area is predominantly influenced by evaporative crystallisation, with calcite, dolomite, gypsum, and halite identified as potential mineral phases.

As shown in Figure 7, the SI values for calcite and dolomite range from 0.73 to 2.15 and 1.66 to 4.81, respectively, indicating that these minerals are in a saturated to supersaturated state in the water samples. This suggests that these minerals exert control over the concentrations of their respective components in the groundwater. In contrast, the SI values for gypsum and halite range from −3.16 to −1.32 and −7.6 to −5.17, respectively. Additionally, from 2020 to 2023, the SI values for these minerals showed a trend towards zero, indicating that they are undersaturated but evolving towards equilibrium. This implies that the dissolution of halite and gypsum will continue, suggesting increased interaction between groundwater and halite/gypsum strata, with an increasing trend expected in the coming years.

The high saturation indices (SI > 0) for calcite and dolomite thermodynamically indicate a strong tendency for precipitation. However, whether this translates into actual scale formation within the mine drainage system is governed by kinetic factors and local hydrochemical conditions. Precipitation kinetics are often sluggish, especially for dolomite, which requires overcoming significant activation energy barriers even under supersaturated conditions [28,29]. In practice, scale formation is not an instantaneous process but requires sufficient induction time for nucleation and crystal growth. Based on monitoring data from 2020 to 2023, the persistent supersaturation of calcite and dolomite establishes the thermodynamic basis for scaling. Although precipitation is kinetically controlled, sustained high SI values (e.g., Dolomite SI often >3.5) can significantly shorten nucleation time, increasing the practical risk of scale formation on rough surfaces such as mine pipes.

Therefore, it is recommended to set Dolomite SI > 4.2 or Calcite SI > 2.3 as primary warning thresholds.

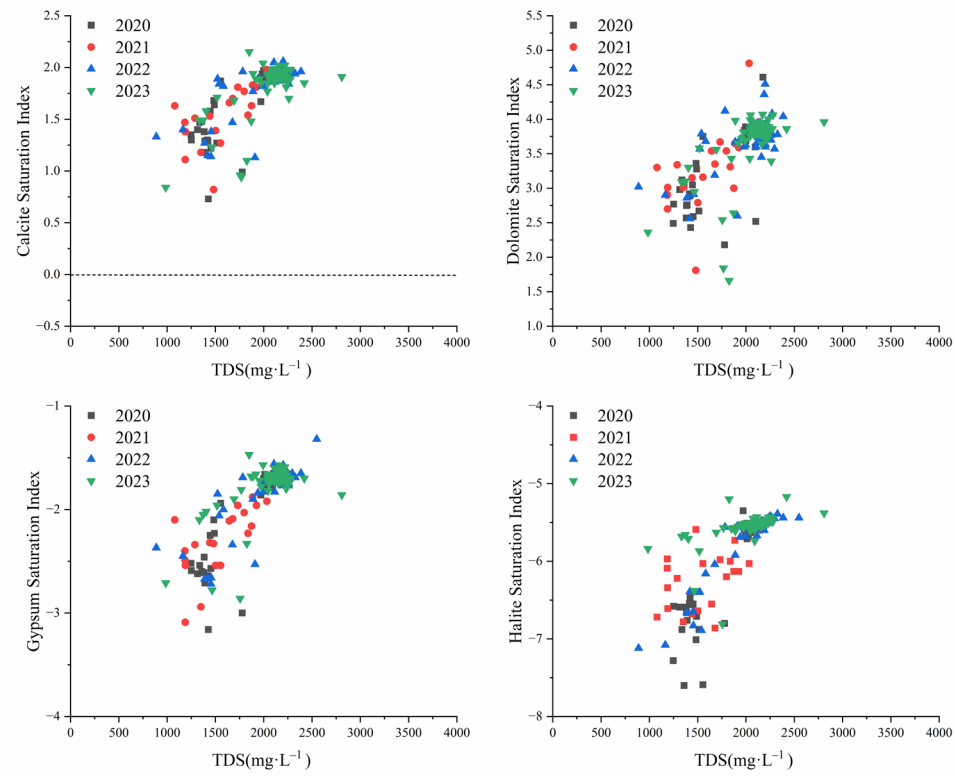


Figure 7. Relationship between saturation indices of major minerals and TDS in the study area.

The saturation index (SI) not only reflects the mineral dissolution-precipitation equilibrium, but its dynamic variation patterns also contain hydrogeological information. By analysing the numerical values, trends, and combined characteristics of different mineral SI values, a dual-function monitoring system can be established to warn against both scaling risks (pipe blockages) and water hazard risks (water inrush).

3.3.5. Principal Component Analysis (PCA)

To further investigate the primary processes controlling the chemical evolution of groundwater, PCA was performed to reduce the dimensionality of various components [30,31], enabling a quantitative assessment of the factors influencing the formation of sandstone water. In the study area, the Kaiser-Meyer-Olkin (KMO) test value for the correlation matrix of six indicators was 0.567, and Bartlett's test of sphericity showed significance ($p < 0.01$), indicating that the data were suitable for PCA. Six conventional hydrochemical indicators ($Na^+ + K^+$, Ca^{2+}, Mg^{2+}, Cl^-, SO_4^{2-}, and HCO_3^-) from the sandstone aquifer were analysed using SPSS. Three principal components (F1, F2, and F3) were extracted using the Varimax rotation method (Table 3), with a cumulative variance contribution rate of 91.894%, effectively explaining the main controlling factors of the sandstone water in the study area.

The rotated component matrix (Table 4) shows that principal component F1, with a variance contribution rate of 66.269%, is highly correlated with Cl^-, $Na^+ + K^+$, SO_4^{2-}, and Ca^{2+}. F1 indicates that evaporite dissolution and evaporative concentration are the dominant processes controlling the overall hydrogeochemical evolution.

Table 3. Total variance explained.

Component	Initial Eigenvalues	% of Variance	Cumulative %
F1	3.976	66.269	66.269
F2	0.899	14.988	81.256
F3	0.638	10.638	91.894
F4	0.315	5.258	97.152
F5	0.158	2.634	99.786
F6	0.013	0.214	100.000

Table 4. Rotated component matrix of sandstone water.

Component	Principal Component		
	F1	F2	F3
Cl^-	0.97	0.108	0.117
Ca^{2+}	0.841	0.474	0.153
$SO_4{}^{2-}$	0.784	0.432	0.166
$Na^+ + K^+$	0.644	0.607	0.084
$HCO_3{}^-$	−0.259	−0.951	−0.069
Mg^{2+}	0.151	0.076	0.985
% of Variance	66.269	14.988	10.638
Cumulative %	66.269	81.256	91.894

Principal component F2, contributing 14.988% of the variance, shows a negative correlation between $SO_4{}^{2-}$ and $HCO_3{}^-$, reflecting the influence of sulfate reduction. This component also suggests that increased CO_2 outgassing in the mining-affected environment could lead to $HCO_3{}^-$ consumption and calcite ($CaCO_3$) precipitation. Thus, F2 represents the impact of mining disturbances on the sandstone aquifer.

Principal component F3, with a variance contribution rate of 10.638%, is primarily associated with Mg^{2+}, which exhibits weak correlation with other ions (Table 2). F3 may indicate the presence of an independent process, possibly the weathering of magnesium-containing minerals [32].

PCA results indicate that the hydrochemical evolution in the study area is primarily controlled by evaporite dissolution, with the combined effects of carbonate equilibrium and silicate weathering. As shown in Figure 8, to deeply analyze the spatial structure of the hydrochemical data, the sample points are projected onto three planes formed by pairs of principal components: the F1-F2 plane (red data points), the F1-F3 plane (blue data points), and the F2-F3 plane (green data points). These colored projection points collectively reveal the distribution patterns and clustering characteristics of all data points in the multidimensional space: from 2020 to 2023, the data points gradually shifted from the third quadrant towards the second quadrant, with increasing F1 and F2 scores. This suggests that the influence of evaporative concentration on the water samples has strengthened, and the impact of mining disturbances on the sandstone aquifer has increased over time. From a temporal perspective, the data points in Figure 8 generally moved in the positive direction of F1 and F2. Regarding F3, the overall scores remained relatively stable from 2020 to 2022 but showed a tendency to cluster towards the positive direction of F3 in 2023.

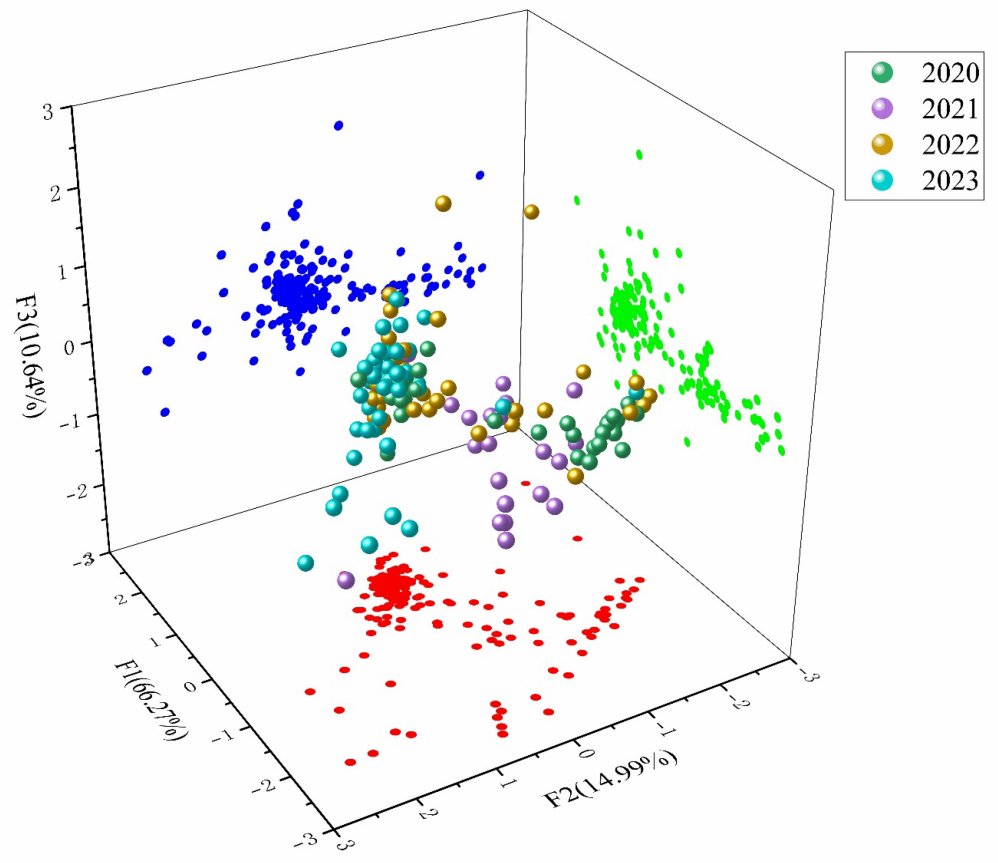


Figure 8. Three-dimensional diagram of sandstone water-load scores.

4. Conclusions

The hydrochemical evolution of the roof sandstone aquifer in the study area represents a dynamic system influenced by multiple hydrogeochemical processes. This system is undergoing a significant trend characterised by a shift from complexity to singularity and continuous salinisation, with mining activities as the primary driver of these changes. The specific conclusions are as follows:

(1) The water samples in the study area are generally weakly alkaline. Although the TDS concentration slightly decreased in 2021, the overall trend from 2020 to 2023 has been a gradual increase. Simultaneously, the hydrochemical type evolved from an initial coexistence of Cl-Na and HCO_3·Cl-Na types in 2020 to a predominantly Cl-Na type in subsequent years.

(2) A strong correlation between $Na^+ + K^+$ and Cl^- in the sandstone water indicates a common source, primarily derived from halite dissolution, with additional contributions from the dissolution of calcium-containing evaporites. Gibbs diagrams demonstrate that the water samples are significantly influenced by evaporative concentration and leaching. Water–rock interaction analysis confirms that evaporite dissolution is the dominant process. Both influences have intensified from 2020 to 2023.

(3) Calcite and dolomite in the water samples are in a saturated or supersaturated state, while gypsum and halite remain undersaturated but show a tendency to dissolve towards equilibrium over time. Changes in water-conducting pathways should be carefully monitored. Currently, the dominant pathways are the fracture networks directly induced by mining activities [33], which facilitate the rapid influx of oxygen and accelerate water–rock interactions. Furthermore, geological surveys indicate that faults extending to the base of the aquifer possess the potential to be reactivated due to

mining disturbance, forming lagging water-conducting channels. The SI of dolomite and calcite can serve as early-warning indicators and should be incorporated into routine water quality monitoring. These indices offer a more dynamic reflection of the system's status compared to single concentration values and can provide a basis for water hazard prevention.

(4) In addition to evaporative concentration and leaching, the hydrochemical characteristics of the Banji roof sandstone aquifer are also influenced by forward cation exchange and sulfate reduction. However, both sulfate reduction and forward cation exchange have gradually weakened over time. These observations suggest that mining activities have significantly disrupted the hydrochemical environment.

Author Contributions: Conceptualization, N.X., Q.L. and Y.L.; methodology, N.X. and Q.J.; validation, N.X. and G.S.; investigation, N.X.; writing—original draft preparation, N.X.; writing—review and editing, Q.L., Y.L. and Q.J. All authors have read and agreed to the published version of the manuscript.

Funding: This research received no external funding.

Institutional Review Board Statement: Not applicable.

Informed Consent Statement: Not applicable.

Data Availability Statement: The original contributions presented in this study are included in the article. Further inquiries can be directed to the corresponding authors.

Acknowledgments: We would like to express our gratitude to our teacher and senior schoolmate for their guidance.

Conflicts of Interest: All authors declare no conflicts of interest.

References

1. Lu, C.; Li, S.; Xu, K.; Liu, J. Coal Mine Safety Accidents, Environmental Regulation and Economic Development—An Empirical Study of PVAR Based on Ten Major Coal Provinces in China. *Sustainability* **2022**, *14*, 14334. [CrossRef]
2. Tang, X.; Wang, Z.; Zhang, W. Mine Roof Water Inflow Prediction Model for the Initial Mining Disturbance Stage Based on Simulation-Driven Feature Selection and Ensemble Learning. *Results Eng.* **2025**, *28*, 106977. [CrossRef]
3. Wang, T.; Shi, J.; Xu, Z.; Zhao, B.; Wu, K. Prediction-Assessment-Optimization of Water Influx in Underground Coal Gasification: A Systematic Method. *Next Energy* **2026**, *10*, 100483. [CrossRef]
4. Li, B.; Wang, G.; Liu, F.; Shi, Z.; Kong, Q.; Zhang, S.; Yan, X.; Liao, F.; Guo, L.; Liu, C. Hydrochemical Characteristics and Evolution of Geothermal Waters in Western Yunnan, China Based on Self-Organizing Map and Hydrogeochemical Simulation. *Appl. Geochem.* **2025**, *181*, 106291. [CrossRef]
5. Wang, P.; Zhang, W.; Zhu, Y.; Liu, Y.; Li, Y.; Cao, S.; Hao, Q.; Liu, S.; Kong, X.; Han, Z.; et al. Evolution of Groundwater Hydrochemical Characteristics and Formation Mechanism during Groundwater Recharge: A Case Study in the Hutuo River Alluvial–Pluvial Fan, North China Plain. *Sci. Total Environ.* **2024**, *915*, 170159. [CrossRef]
6. Sharma, M.K.; Kumar, P.; Prajapati, P.; Bhanot, K.; Wadhwa, U.; Tomar, G.; Goyal, R.; Prasad, B.; Sharma, B. Study of Hydrochemical and Geochemical Characteristics and Solute Fluxes in Upper Ganga Basin, India. *J. Asian Earth Sci. X* **2022**, *8*, 100108. [CrossRef]
7. Tian, J.; Wang, Z.; Daskalopoulou, K.; Zhang, M.; Huo, Y.; Cao, Y.; Yang, J.; Liu, W.; Liu, J.; Xu, S. Hydrochemical Characteristics, Driving Factors and Health Risk of Fluoride in Groundwater from the Northwestern Ordos Basin, China. *Geosci. Front.* **2025**, *16*, 102123. [CrossRef]
8. Jiang, Q.; Liu, Q.; Liu, Y.; Zhu, J.; Chai, H.; Chen, K. Chemical Composition of Groundwater and Its Controlling Factors in the Liuzhuang Coal Mine, Northern Anhui Province, China. *Water Supply* **2023**, *23*, 4937–4956. [CrossRef]
9. Yuan, L.; Shen, P.; Zhang, J.; Yang, J.; Kong, X. Hydrochemical Zonation and Geochemical Processes of Geothermal Water in Beijing. *Geothermics* **2025**, *128*, 103273. [CrossRef]
10. Liu, F.; Wang, G.; Liang, X.; Qu, S.; Shi, Z.; Li, J.; Luo, A. Temporal Variation of Groundwater Hydrochemistry and Water Stable Isotopes under Long-Term Mining Disturbance in a Coal Mine, Northwest China. *Appl. Geochem.* **2023**, *158*, 105802. [CrossRef]
11. Shuaibu, A.; Kalin, R.M.; Phoenix, V.; Banda, L.C.; Lawal, I.M. Hydrogeochemistry and Water Quality Index for Groundwater Sustainability in the Komadugu-Yobe Basin, Sahel Region. *Water* **2024**, *16*, 601. [CrossRef]

12. *DZ/T 0064.80-1993*; Methods for Examination of Groundwater Quality—Determination of 39 Elements including Lithium by Plasma Mass Spectrometry. Standards Press of China: Beijing, China, 1993.
13. *MT/T 672-1997*; Analytical Methods for Water Chemistry in Coal Mine Water Hazard Prevention and Control. Standards Press of China: Beijing, China, 1997.
14. Shen, J.; Huang, T.; Zhang, H.; Lin, W. Hydrochemical and Isotopic Characteristics of Water Sources for Biological Activity across a Massive Evaporite Basin on the Tibetan Plateau: Implications for Aquatic Environments on Early Mars. *Sci. Total Environ.* **2024**, *935*, 173442. [CrossRef] [PubMed]
15. Phuyal, P.; Ranabhat, S.; Khatri, S.; Lamichhane, N.; Pant, R.R.; Thapa, L.B.; Prasad Yadav, R.K. Hydrochemical Characteristics, Water Quality and Diatom Assemblage in Dordi River, Nepal. *Watershed Ecol. Environ.* **2025**, *7*, 23–35. [CrossRef]
16. Dong, F.; Yin, H.; Cheng, W.; Li, Y.; Qiu, M.; Zhang, C.; Tang, R.; Xu, G.; Zhang, L. Study on Water Inrush Pattern of Ordovician Limestone in North China Coalfield Based on Hydrochemical Characteristics and Evolution Processes: A Case Study in Binhu and Wangchao Coal Mine of Shandong Province, China. *J. Clean. Prod.* **2022**, *380*, 134954. [CrossRef]
17. Jia, W.; Liu, K.; Yan, J.; Zhang, Y.; Tong, J.; Yu, K.; Zhang, S.; Wang, L.; Yu, C. The Difference in Hydrochemical Characteristics of Geothermal Water between the Eastern and Western Parts of the Wugongshan Area and Its Genetic Mechanism. *J. Geochem. Explor.* **2024**, *266*, 107575. [CrossRef]
18. Cao, Z.; Qian, H.; Gao, Y.; Li, K.; Shi, X.; Li, S.; Tian, P.; Liu, Y.; Zhang, J.; Shi, Z.; et al. Hydrochemical Evolution and Surface Water-Groundwater Interactions in a Typical Mountainous Basin: Insights from Multiple Isotopes, Chemical Tracers, and Multiple Models. *J. Environ. Chem. Eng.* **2026**, *14*, 120611. [CrossRef]
19. Dogramaci, S.; Wallis, I.; Cook, P.; Kneeshaw, A. Hydrochemical Evolution of Groundwater in a Semi-Arid Environment Verified through Natural Tracer and Geochemical Modelling, Northwest Australia. *Appl. Geochem.* **2025**, *183*, 106337. [CrossRef]
20. Zhan, H.; Liu, S.; Wu, Q.; Liu, W.; Shi, L.; Liu, D. Effects of Deep Coal Mining on Groundwater Hydrodynamic and Hydrochemical Processes in a Multi-Aquifer System: Insights from a Long-Term Study of Mining Areas in Ecologically Fragile Western China. *J. Contam. Hydrol.* **2024**, *265*, 104386. [CrossRef]
21. Jeong, C.; Jeon, W.-H.; Kim, D.-H.; Song, S.M.; Lee, J.-Y.; Hyun, S.P.; Moon, H.S. Effect of Rainfall on Spatiotemporal Variation of Hydrochemical and Isotopic Characteristics of the Coastal Lagoon (Songjiho) and Groundwater in Korea. *J. Hydrol. Reg. Stud.* **2025**, *58*, 102303. [CrossRef]
22. Yu, X.; Wang, J.; Zhang, Z.; Liao, Z.; Guo, J. Hydrochemical, Isotopic, and Geophysical Methods for Better Understanding the Evolutionary Characteristics of Sustainable Yield during Different Groundwater Extraction Stages in Two Wellfields of the Sunite Paleochannel, China. *J. Hydrol. Reg. Stud.* **2025**, *60*, 102608. [CrossRef]
23. Liu, J.; Gao, Z.; Feng, J.; Wang, M. Identification of the Hydrochemical Features, Genesis, Water Quality and Potential Health Hazards of Groundwater in Dawen River Basin, North China. *Ecol. Indic.* **2023**, *149*, 110175. [CrossRef]
24. Liu, J.; Gao, M.; Wang, T.; Yang, J.; Wang, Q. Hydrochemical Processes and Groundwater Quality Assessment in Yushenfu Mining Area, Northwest China. *Desalination Water Treat.* **2019**, *165*, 177–187. [CrossRef]
25. Basharat, U.; Zhang, W.; Abbasi, A.; Mahroof, S.; Han, C.; Khan, S.H.; Li, S. Integrated Assessment of Groundwater Hydrogeochemistry and Quality Using Multivariate Statistical Analysis, Self-Organizing Maps, and Water Quality Indices in District Bagh, AJK, Pakistan. *Ecotoxicol. Environ. Saf.* **2025**, *301*, 118515. [CrossRef] [PubMed]
26. Sidhu, N.; Kaur, L.; Rishi, M.S.; Din, S.N.U.; Tewari, K.; Singh, P. Integrating Multivariate Hydrogeochemical Analysis with Human Health Risk Assessment: An Inverse Geochemical and Statistical Modeling Approach. *J. Geochem. Explor.* **2024**, *258*, 107389. [CrossRef]
27. Ren, X.; Zhang, Z.; Yu, R.; Li, Y.; Li, Y.; Zhao, Y. Hydrochemical Variations and Driving Mechanisms in a Large Linked River-Irrigation-Lake System. *Environ. Res.* **2023**, *225*, 115596. [CrossRef]
28. Pietzsch, R. A Global Assessment of the Geochemistry of Carbonate Mineral Formation and the Dynamics of Calcite Precipitation in Alkaline Lakes. *Earth-Sci. Rev.* **2026**, *272*, 105347. [CrossRef]
29. Petrash, D.A.; Bialik, O.M.; Bontognali, T.R.; Vasconcelos, C.; Roberts, J.A.; McKenzie, J.A.; Konhauser, K.O. Microbially Catalyzed Dolomite Formation: From near-Surface to Burial. *Earth-Sci. Rev.* **2017**, *171*, 558–582. [CrossRef]
30. Chalise, B.; Paudyal, P.; Kunwar, B.B.; Bishwakarma, K.; Thapa, B.; Pant, R.R.; Neupane, B.B. Water Quality and Hydrochemical Assessments of Thermal Springs, Gandaki Province, Nepal. *Heliyon* **2023**, *9*, e17353. [CrossRef]
31. Ganguli, S.; Rifat, A.H.; Howlader, S.; Hasan, A.; Islam, S.; Alam, M.E.; Islam, N. Assessment of Bhatiari Lake Water Quality: Pollution Indices, Hydrochemical Signatures and Hydro-Statistical Analysis. *J. Indian Chem. Soc.* **2022**, *99*, 100585. [CrossRef]

32. Bhuiyan, M.K.; Roy, H.; Saidur Rahman, K.; Nath Roy, B.; Bhuyan, A.A.K.; Jahedi, R.M.; Islam, S. Development of a PCA-Derived Water Quality Index Model for Monitoring the Urban River Systems in Dhaka City, Bangladesh. *City Environ. Interact.* **2026**, *29*, 100276. [CrossRef]
33. Okamoto, K.; Aoyagi, N.; Mukuhira, Y.; Asanuma, H. Monitoring Fluid Flows without Seismicity Associated with Continuous Water Injection into Geothermal Reservoirs. *Int. J. Rock Mech. Min. Sci.* **2025**, *195*, 106290. [CrossRef]

Disclaimer/Publisher's Note: The statements, opinions and data contained in all publications are solely those of the individual author(s) and contributor(s) and not of MDPI and/or the editor(s). MDPI and/or the editor(s) disclaim responsibility for any injury to people or property resulting from any ideas, methods, instructions or products referred to in the content.